communications materials

A Nature Portfolio journal

Article

https://doi.org/10.1038/s43246-025-00952-7

# Signatures of Kramers-Weyl fermions in the charge density wave material $(TaSe_4)_2I$



Soyeun Kim[1,2,3,10], Robert C. McKay[4,10], Nina Bielinski[1,2,10], Junehu Park[2,5,6], Chengxi Zhao[2,5], Meng-Kai Lin[1,2,7], Joseph A. Hlevyack[1,2], Xuefei Guo[1,2], Sung-Kwan Mo[8], Peter Abbamonte[1,2], T.-C. Chiang[1,2], André Schleife[2,5,9], Daniel P. Shoemaker[2,5], Barry Bradlyn[4] ✉ & Fahad Mahmood[1,2] ✉

The quasi-one-dimensional charge density wave (CDW) material $(TaSe_4)_2I$ has been recently predicted to host Kramers-Weyl (KW) fermions which should exist in the vicinity of high symmetry points in the Brillouin zone in chiral materials with strong spin-orbit coupling. However, direct spectroscopic evidence of KW fermions is limited. Here we use helicity-dependent laser-based angle-resolved photoemission spectroscopy (ARPES) in conjunction with tight-binding and first-principles calculations to identify KW fermions in $(TaSe_4)_2I$. We find that topological and symmetry considerations place distinct constraints on the (pseudo-) spin texture and the observed spectra around a KW node. Our findings highlight the unique topological nature of $(TaSe_4)_2I$ and provide a pathway for identifying KW fermions in other chiral materials.

The past decade has seen the prediction and discovery of a large number of topological materials, including 3D topological insulators[1,2], Dirac[3,4] and Weyl semimetals[5–8], and multifold chiral semimetals[9–14]. These materials are characterized by nontrivial topology in the electronic band structure. They are typically identified using a combination of *ab—initio* calculations and symmetry-based methods that help to isolate unique spectroscopic features (such as Dirac and Weyl fermions) at certain points and lines in the Brillouin zone (BZ). In many cases, these topological fermions arise due to the presence of certain crystalline symmetries[15–19].

Recently, however, it has been realized that chiral crystals, characterized by the absence of orientation-reversing symmetries, with strong spin-orbit coupling (SOC) universally host topological Kramers-Weyl (KW) fermions[20]. In these materials, each time-reversal invariant momentum (TRIM) point in the BZ must feature a topologically charged Weyl point (or multifold fermion, if there are additional crystal symmetries) and is referred to as a KW point. Electronic bands near the KW point are split by SOC in all directions, forming pockets with opposite Chern numbers and an approximately radial (monopole-like) spin texture. Other novel features of these KW fermions include the circular photogalvanic effect[10,21–24] and a longitudinal magneto-electric response[25–27].

As highlighted in ref. 20, a number of chiral crystals are predicted to host KW fermions, yet experimental confirmation remains elusive. This is primarily because the KW nodes are often far from a material's Fermi level and can also be in close proximity to other symmetry-enforced Weyl nodes. For example, ref. 20 predicted that the chiral charge density wave (CDW) compound $(TaSe_4)_2I$[28,29] hosts KW nodes at its $N$ TRIM point but at an energy above its Fermi level. $(TaSe_4)_2I$ has also gained extensive interest recently as a Weyl-CDW candidate whereby its Fermi surface Weyl points (FSWP) are gapped by the onset of CDW correlations below the CDW transition temperature $T_{CDW}$[30]. Experimental observation of novel magneto-electric responses under an external magnetic field suggested the $(TaSe_4)_2I$ as a first condensed matter version of an axionic insulator[31,32], which is under active debate[33]. Spurred by these aforementioned findings, exploration of the unique combination of physical properties $(TaSe_4)_2I$ hosts was rejuvenated, motivating further state-of-the-art experiments[34–38].

Here, we use helicity-dependent laser ARPES, in combination with a tight-binding model and first-principles calculations to observe distinctive

[1]Department of Physics, The Grainger College of Engineering, University of Illinois Urbana-Champaign, Urbana, IL, USA. [2]Materials Research Laboratory, The Grainger College of Engineering, University of Illinois Urbana-Champaign, Urbana, IL, USA. [3]Department of Physics and Chemistry, Daegu Gyeongbuk Institute of Science and Technology (DGIST), Daegu, South Korea. [4]Department of Physics and Institute for Condensed Matter Theory, The Grainger College of Engineering, University of Illinois Urbana-Champaign, Urbana, IL, USA. [5]Department of Materials Science and Engineering, The Grainger College of Engineering, University of Illinois Urbana-Champaign, Urbana, IL, USA. [6]National Center for Supercomputing Applications, University of Illinois Urbana-Champaign, Urbana, IL, USA. [7]Department of Physics, National Central University, Taoyuan, Taiwan. [8]Advanced Light Source, Lawrence Berkeley National Laboratory, Berkeley, CA, USA. [9]National Center for Supercomputing Applications, University of Illinois at Urbana-Champaign, Urbana, IL, USA. [10]These authors contributed equally: Soyeun Kim, Robert C. McKay, Nina Bielinski. ✉e-mail: bbradlyn@illinois.edu; fahad@illinois.edu

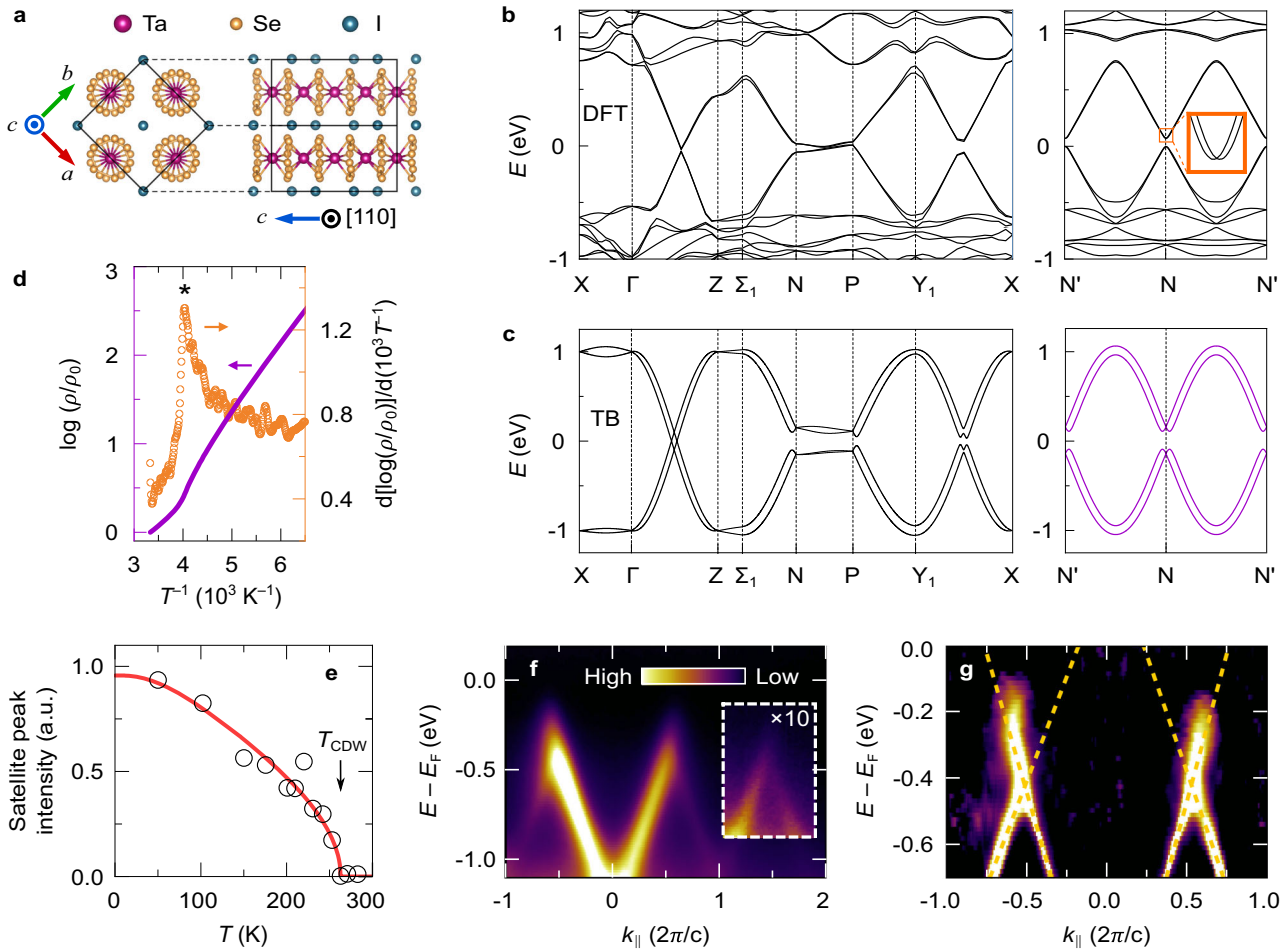


**Fig. 1 | Crystal structure, experimental characterization, and Kramers-Weyl (KW) band structure of $(TaSe_4)_2I$. a** Crystal structure as seen from the (001) and (110) directions. Here (001) is along the Ta chain direction and (110) is the natural cleavage plane. A (conventional) unit cell is indicated by solid lines. **b**, **c** Electronic band structure of $(TaSe_4)_2I$ as calculated using **(b)** density functional theory (DFT) and **(c)** a tight-binding model (TB) described in the SI[46]. The KW crossing along the N′-N-N′ path is shown in the right panels. **d** The logarithmic resistivity normalized by $\rho_0 = \rho(300\ \mathrm{K})$. **e** Temperature dependence of the CDW satellite peaks (symbols) from the Bragg reflection at $(h, k, l) = (-1, 3, 4)$. $T_{CDW} \sim 260$ K is marked with an arrow. See Fig. S5 for the line cuts of satellite peaks[46]. A solid line is a fit using a BCS gap function. **f, g** ARPES plots measured with 50 eV photon energy at room temperature, showing **(f)** the photoemission intensity and **(g)** the curvature taken parallel to the ΓZ (chain) direction. The intensity is rescaled by 10 inside the dashed box in **(f)**. Dashed straight lines in **(g)** are guides to the eye.

signatures that may indicate the presence of KW fermions in the chiral CDW compound $(TaSe_4)_2I$. Note that the surface of $(TaSe_4)_2I$ is intrinsically n-doped due to iodine vacancies, which raise its chemical potential as observed in previous photoemission experiments[39]. We take advantage of this to isolate conduction band features around the *N* TRIM point. We find that the helicity-dependent photoemission intensity is directly correlated with the unique (pseudo-)spin texture around this TRIM point, which confirms the presence of KW fermions in $(TaSe_4)_2I$.

## Results and discussion

### Sample characterization of $(TaSe_4)_2I$

$(TaSe_4)_2I$ has been studied extensively as a model quasi-one-dimensional system undergoing a CDW Peierls transition[40–42]. As shown in Fig. 1a, $(TaSe_4)_2I$ consists of chains of Ta atoms surrounded by Se atoms along the *c*-axis. The chains are bonded weakly by I atoms, forming a needle-like crystal that naturally cleaves along the (110) plane. The unit cell size of $(TaSe_4)_2I$ is $(a, b, c) = (9.5373(9), 9.5373(9), 12.770(2))$ Å$^{-1}$[43]. In Fig. 1b we show the band structure of $(TaSe_4)_2I$, computed using density functional theory (DFT). The left panel shows the bands along high-symmetry lines, and is consistent with known literature[15,20,30]. In the right panel, we show the bands along the experimentally relevant path and expressed with respect to the crystallographic axes $(k_a, k_b, k_c) = (\pi/a, 0, k_c)$, with the N point at $k_c = \pi/c = 0.246$ Å$^{-1}$, and the N′ point at $k_c = -\pi/c$. In Fig. 2a we describe our coordinate system, and how it maps to the crystallographic axes, defining $k_{\parallel}$, $k_{\perp,n}$ as parallel/perpendicular with respect to the Ta chain direction. We see in the inset that there is a small spin-orbit splitting visible, exposing a KW fermion at the N TRIM point. To facilitate further theoretical calculations of photoemission intensity, we use this DFT input to construct a symmetry-inspired four-band tight-binding model. We use techniques from topological quantum chemistry[44] to ensure this model reproduces the symmetry properties of the four bands closest to the Fermi level, as determined in the Topological Materials Database[45]. Details of the model can be found in the SI[46]. The spectrum of the tight-binding model is shown in Fig. 1c. We see good qualitative agreement with the DFT spectrum, although we have artificially increased the SOC strength in the tight-binding model for clarity.

We first characterized our samples by measuring the four-terminal electrical resistivity $\rho$ as a function of temperature $T$ with the current applied along the *c*-axis. Consistent with previous work[31], $\rho$ increases with decreasing $T$ and its logarithmic derivative shows a peak around the expected CDW transition temperature of $T_{CDW} \sim 260$ K (Fig. 1d). Moreover, the logarithmic derivative saturates around a value of 0.7 ($10^{-3}$ K), corresponding to a gap size of 250 meV. This is also consistent with previous transport experiments[31].

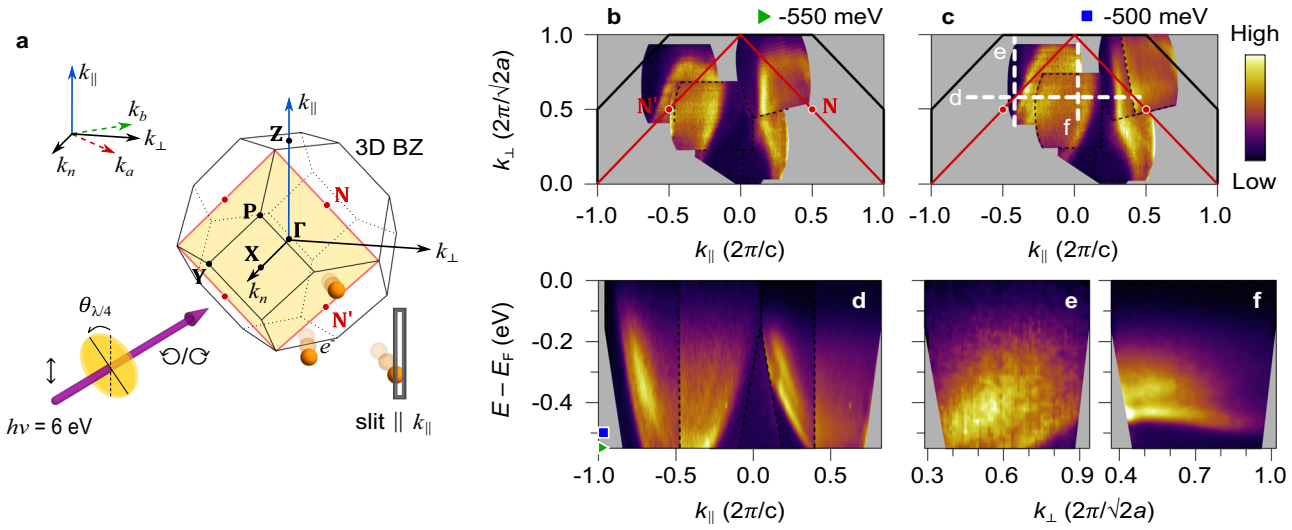


**Fig. 2 | Laser-ARPES measurements on $(TaSe_4)_2I$ using a photon energy of $h\nu = 6$ eV taken at 280 K. a** Measurement geometry in relation to the 3D Brillouin zone (BZ). $k_a/k_b$ is the crystal $a/b$ direction. $k_{\parallel}/k_{\perp,n}$ is parallel/perpendicular to the Ta chain direction. The (110) cleavage plane corresponding to $k_n = 0.5$ $(2\pi/\sqrt{2}a)$ is highlighted as the shaded plane. The light helicity is adjusted by rotating the fast axis of the $\lambda/4$ quarter waveplate ($\theta_{\lambda/4}$). **b**, **c** Constant energy maps taken at (**b**) $E - E_F = -550$ meV and at (**c**) $E - E_F = -500$ meV, summed over 20 meV. **d**–**f** Energy-momentum cuts along the white lines shown in (**c**).

To further characterize the CDW order, we also performed X-ray diffraction (XRD) as a function of temperature above and below $T_{CDW}$. Similar to observations from other scattering studies[47,48], satellite peaks corresponding to $q_{CDW}$ emerge for $T < T_{CDW}$ (see Fig. S5 in ref. 46). The intensities of the CDW peaks follow the expected mean-field behavior with $T_{CDW} \sim 260$ K, as can be seen in Fig. 1e. We also performed synchrotron-based ARPES experiments with a photon energy of 50 eV on the same set of samples to compare with previous such experiments. Figure 1f shows the in-plane band dispersion at room temperature along the chain direction (in this case the ΓZ-direction). We observe the characteristic linearly dispersing valence bands with a minimum at Γ as theoretically predicted and seen by various ARPES experiments[30,39,42,49]. Note that the valence band maximum is significantly below the chemical potential, indicating the intrinsic n-doping of $(TaSe_4)_2I$ samples. At these high photon energies, the photoemission intensity for the conduction bands is much weaker compared to that of the valence bands[30]. Nonetheless, the conduction band can be clearly resolved in the ARPES curvature plots, as shown in Fig. 1g and the overall shape of the bands is consistent with our laser ARPES experiments (discussed below).

## Laser ARPES measurements

Our laser ARPES experimental configuration is shown in Fig. 2 along with the bulk 3D BZ. For a photon energy of 6 eV, photoemission primarily originates from the plane corresponding to $k_n \sim 0.6\,(2\pi/\sqrt{2}a)$[46]. This plane is close to the high symmetry $N$ points, as indicated by the shaded plane in Fig. 2a. For our measurements, the sample is aligned such that the Ta chains are parallel to the analyzer slit which gives energy as a function of $k_{\parallel}$ for a given scan. The sample is then rotated so that $k_{\perp}$ is close to the momentum of the N′ TRIM point. Changes in $k_{\perp}$ around this point are measured by using electronic deflection without sample rotation. We first show constant energy ARPES maps corresponding to energies $E - E_F = -550$ and $-500$ meV in Fig. 2b, c, respectively. As shown in Fig. 2b, two bands are observed around the KW node at the N′ TRIM point, i.e., around the coordinate $(k_{\parallel}, k_{\perp}) = (-0.5, 0.5)$ in units of $(-2\pi/c, 2\pi/\sqrt{2}a)$. These bands disperse outward with increasing kinetic energy, i.e., decreasing binding energy, indicating that they correspond to the conduction band of $(TaSe_4)_2I$ near the KW node at the N′ TRIM point when compared with first-principles calculations and our tight-binding model (Fig. 1b, c). The almost linearly dispersing 'V-shaped' conduction bands are seen more clearly in the energy vs. momentum ($k_{\parallel}$) cut (see Fig. 2d for a plot along the white lines illustrated in 2c). Similar 'V-shaped' bands with relatively high velocities were also resolved in refs. 30 and[39] for momentum along $k_{\parallel}$. On the other hand, for momentum along $k_{\perp}$ (Fig. 2e, f), the bands have a relatively flat dispersion. These weakly dispersing bands along the $k_{\perp}$ direction are a characteristic feature of $(TaSe_4)_2I$ due to its one-dimensional nature and have been observed in a number of previous ARPES studies[39,42,49]. We note that in our ARPES data, the spectral weight near the Fermi level is strongly suppressed compared to that of a reference sample (Au or $Bi_2Se_3$) due to the incoherent nature of the band[50]. The top of the occupied bands is about 100 meV below μ. As established in early ARPES works[50,51], this is due to a strong polaronic effect which makes the spectral weight near the chemical potential incoherent.

## Bands near the KW point

Figure 3a presents the band structure near the $N$ points calculated from the DFT, where the binding energy of the $N$ points is set to 0 eV. The band structure across $k_{\parallel}$ (Fig. 3b) resembles an hourglass shape. It leaves a periodic wavy projection that originates from the interchain coupling[42] in the constant energy cuts (Fig. 3c–e). Overall, the calculation plots above $E = 0$ eV are consistent with the upper 'V-shaped' band and a small band splitting in the experiment (Fig. 2).

Having located the conduction bands originating from a predicted KW node in $(TaSe_4)_2I$, we now characterize their spin texture using helicity-dependent laser ARPES measurements. In general, KW nodes can be distinguished from conventional band-inversion Weyl nodes[20] or the Rashba-like surface band splitting that can arise from iodine vacancy on the top surface[39] by their spin texture. Construction of any Fermi surface enclosing a single KW fermion maps onto itself under time-reversal symmetry. Since time-reversal also flips spin, this constrains the electronic states on opposite sides of the Fermi surface around a KW node to have opposite spin. Note that this is in contrast to a conventional Weyl semimetal arising from band inversion, where there are no symmetry constraints on states at a single Fermi surface. The presence of additional rotational symmetries can further constrain the spins of states near the KW node; in the isotropic limit, we expect to see an approximately radial spin texture arising from the dominant $\boldsymbol{k} \cdot \boldsymbol{\sigma}$ term in the KW Hamiltonian. This was recently observed in spin-resolved ARPES experiments near the KW points in elemental tellurium[52,53]. A similar approximately radial spin texture is expected around KW nodes of

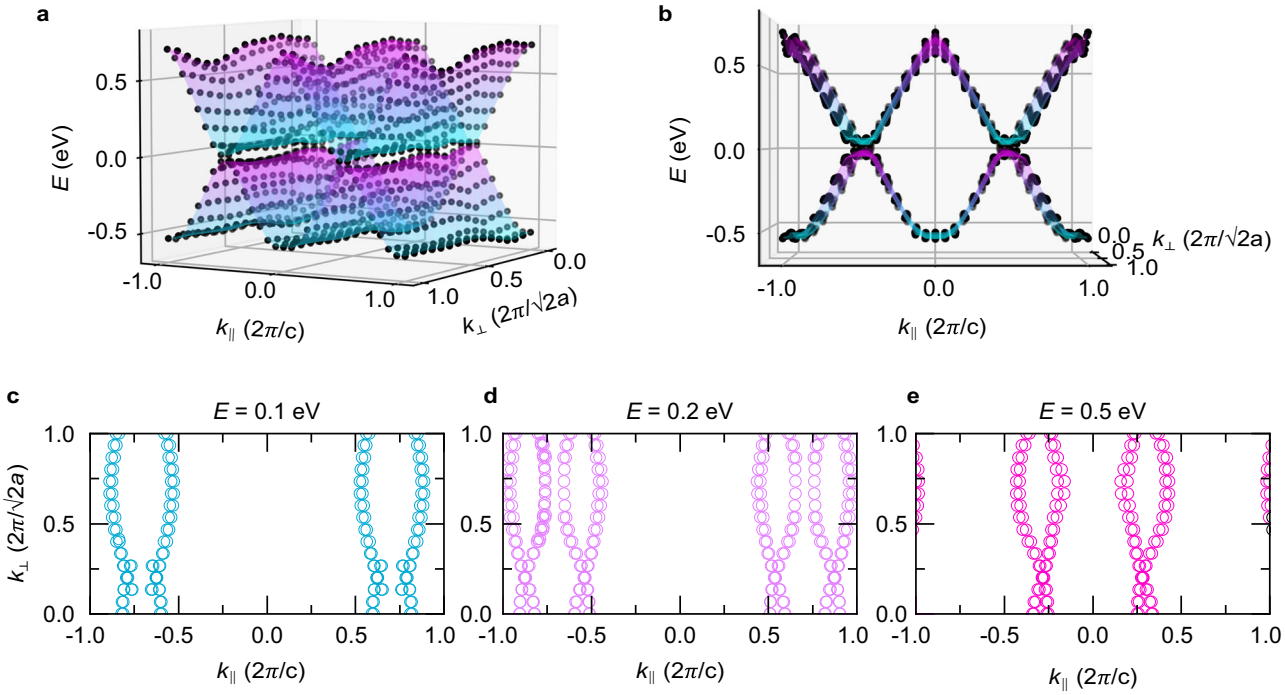


**Fig. 3 | DFT calculation on $(TaSe_4)_2I$ near N points. a, b** 3D band structure shown in different perspective view angles. $k_{\parallel}/k_{\perp}$ is parallel/perpendicular to the Ta chain direction. **c–e** Constant energy cuts at energy **c** 0.1 eV, **d** 0.2 eV, and **e** 0.5 eV above the N point ($E = 0$ eV).

$(TaSe_4)_2I$, albeit with a stronger anisotropy due to its quasi-one-dimensional band structure[46].

### Helicity dependence near KW point

Due to the nature of the spin texture around the observed N′ KW point, we expect a distinctive asymmetry in the helicity-dependent photoemission from bands on either side of this point. Since the crystal is chiral and therefore lacks simple selection rules for ARPES transition matrix elements, we utilized an effective one-step model of photoemission to calculate the ARPES intensity from a tight-binding model. We used our tight-binding model to construct a large finite slab consisting of one region with zero chemical potential (the "inside" of the material) and one region with a large positive chemical potential (the "vacuum"). As an approximation, we modeled the final state of the photoelectron as a time-reversed low energy electron diffraction (TR-LEED) state, where to a first approximation we treated the material-vacuum interface as a step potential. Note that given the low photon energy (6 eV) used in our photoemission experiment, the quantitative features of the dichroic signal will depend on the final-state which can deviate from that of a simple free electron-like state. Thus, accurately computing the dichroic signal would require advanced Green's function and ab initio calculations of the final electron states in the band-structure. Such a calculation is beyond the scope of the present work. Nevertheless, any observed sign reversal with opposite helicity can provide strong evidence for the KW band, regardless of the details of final electron state. We included a phenomenological decay length for the final state inside the sample to account for scattering processes. Since the final state decays inside the sample, and the initial state decays outside the sample, our large finite slab gives a good approximation to a semi-infinite slab. The experimental geometry was taken into full account for the photoemission intensity. Full details on the calculation are given in the SI[46].

The results are illustrated in Fig. 4a–d. Figure 4c, d show the calculated photoemission intensity as a function of light-helicity on the left and right side of the N′ point respectively, as shown in Fig. 4a. Note that there is a clear difference in the photoemission intensities for opposite helicities of light on one side of the N′ point but not on the other. We attribute this to a combination of the chirality of the crystal and the incidence angle of the applied light. Since the crystal is chiral, electronic states on the two sides of the N′ point are related by a twofold rotation symmetry and by time-reversal symmetry. Both of these symmetry operations change the polarization and incidence angle of the incoming light, leading to an asymmetry in the photoemission matrix elements.

To study if this is indeed the case, we modulated the light-helicity of the photoemitting beam using a quarter waveplate (angle denoted by $\theta_{\lambda/4}$). We isolate the bands around the N′ point (Fig. 4e) and plot the integrated spectral intensity in each band (region of integration is shown by the dashed contours in Fig. 4f1–h1) as a function of $\theta_{\lambda/4}$. The results are shown in Fig. 4f2–h2. The photoemission helicity dependence on one side of the KW point (Fig. 4f2, g2) is significantly more asymmetric than the other side (Fig. 4h2) in agreement with theoretical predictions (Fig. 4c, d). In addition, the spin-split bands on opposing sides of the N′ point have opposite helicity-dependence. There is a clear difference in the observed intensity between left and right circularly polarized light as shown in Fig. 4f2, g2 (The spin-split bands can clearly be identified in the EDC cuts in Fig. 4f2, g2). Additional observations of circular dichroism ARPES in $(TaSe_4)_2I$, at a photon energy of 47 eV, are reported in ref. 39. Our observation of helicity-dependence of spin-split bands near the N′ point could potentially also explain the character of the CD-ARPES spectra discussed in that experiment. In addition, each of the spin-split bands on one side of the N′ point has the same helicity dependence whereas that is not the case for the opposite side. There is a clear difference in the observed intensity between left and right circularly polarized light as shown in Fig. 4f2, g2 (The spin-split bands can clearly be identified in the EDC cuts in Fig. 4f2, g2). These observations are a direct consequence of the presence of KW fermions in $(TaSe_4)_2I$ and might also explain the observed circular dichroism in other photoemission experiments on $(TaSe_4)_2I$ using higher photon energies[39].

We note here that the $\theta_{\lambda/4}$-dependence of the photoemission intensity near a KW point of $(TaSe_4)_2I$ is uniquely related to the radial (pseudo-)spin texture around the KW point and is quite different from other well-studied systems, such as topological insulators and strong Rashba SOC materials with a tangential spin texture[54–58]. For those systems, circular dichroism (CD-ARPES) experiments are typically performed to measure the photoemission intensity difference between left and right circularly polarized light

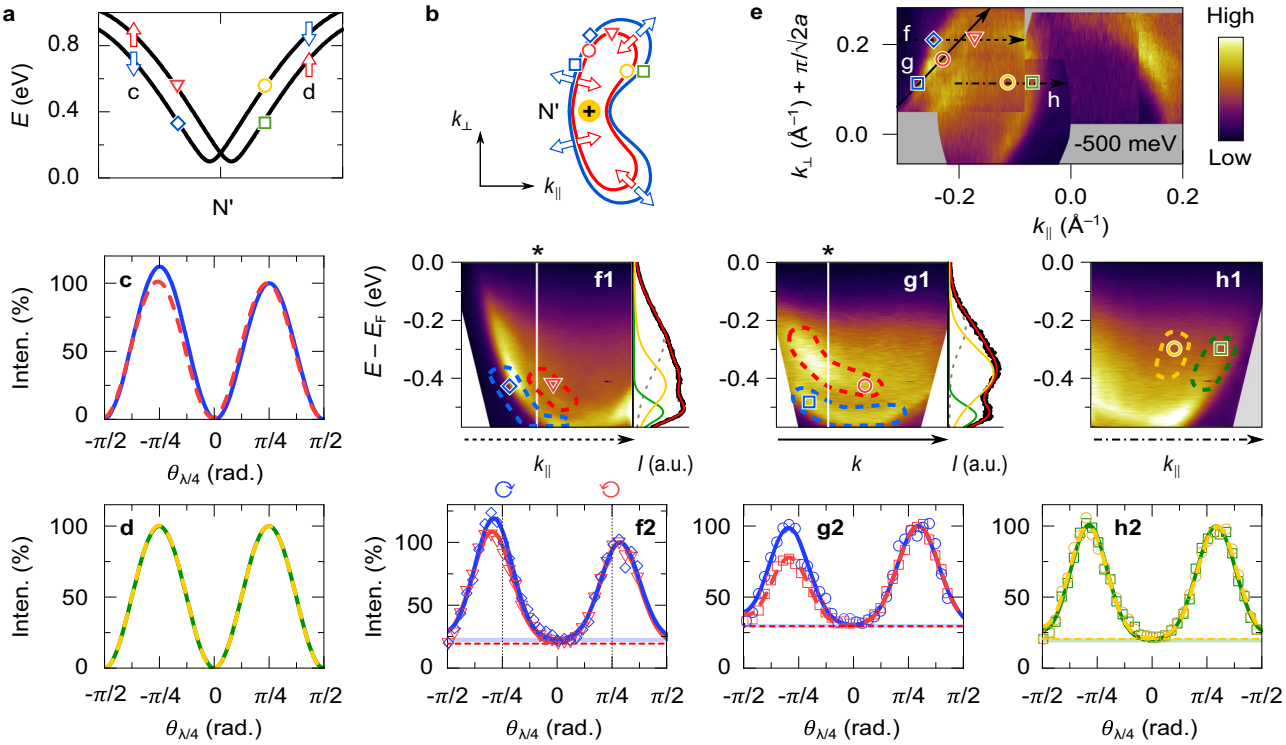


**Fig. 4 | Light helicity dependent ARPES around the N point in $(TaSe_4)_2I$.** **a** Calculated tight-binding (TB) model band structure near the N′ point along the *N*-N′-*N* path. Each Kramers-pair band is separated by spin-orbit coupling (SOC) except at the TRIM (time-reversal invariant momentum) point. Arrows indicate up/down (pseudo-)spin. **b** Sketch of a constant energy map and the (pseudo-)spin texture around the *N* KW point. **c**, **d** Calculated $\lambda/4$ waveplate angle ($\theta_{\lambda/4}$) dependence of photoemission intensities in the TB model for bands to the left (**c**) and right (**d**) of the N′ point as shown in (**a**) and accounting for different measurement geometries. (Pseudo-)spin-up (down) bands that are located at higher (lower) energy are shown as dashed (solid) lines. **e** ARPES constant energy cut measured around the N′ point at $E - E_F = -500$ meV. **f1–h1** ARPES spectra ($E - E_F$ vs. $k$) along the arrows marked in (**d**). Energy distribution curves (at momentum marked with an asterisk) fitted with Voigt functions are displayed on the right side of f1 & g1. **f2–h2** Integrated photoemission intensity as a function of $\theta_{\lambda/4}$ for each spin split band around the N point. The region of integration is shown by the dashed lines in (**f1–h1**). The photoemitting beam helicity is left or right-handed circular polarization at $\theta_{\lambda/4} = +\pi/4$ and $-\pi/4$ radians, respectively. Experimental data (symbols) are normalized to maximum intensity for $\theta_{\lambda/4} > 0$. Solid lines are guides to the eye.

which in turn gives a measure of the pseudospin texture[59]. In particular, ref. 39 reports the CD-ARPES spectra of $(TaSe_4)_2I$ at the iodine-deficient surface where the Rashba-type Dirac band splitting with tangential spin textures are expected. To compare our helicity dependent measurements on bulk bands of $(TaSe_4)_2I$ with those on a system with a tangential pseudo spin texture, we studied the prototypical topological insulator $Bi_2Se_3$ (see Fig. S4 in ref. 46 for more details) with our setup. As observed in previous measurements[54–56,59], we obtain a symmetric $\theta_{\lambda/4}$ dependence of the photoemission intensity at points on either side of the Dirac point. This is in contrast to the asymmetric intensity observed in $(TaSe_4)_2I$ for bands near the N′ point.

### Relevance to the CDW phase

The helicity dependence below the CDW transition is of interest, though experimentally hindered by strong polaronic effects near the Fermi level[50]. KW fermions, protected at TRIM points in chiral space groups, are expected to persist across $T_{CDW}$, as $(TaSe_4)_2I$ remains chiral above and below the transition[43,60,61]. However, in contrast to the FSWP case in ref. 30, no CDW wavevector connecting TRIM points is observed, making the coupling of KW pairs unlikely.

## Conclusions

In conclusion, by using helicity-dependent APRES, ab-initio calculations, and tight-binding modeling, we have investigated the KW fermions at the N point of $(TaSe_4)_2I$. Our work provides the first experimental evidence for the presence of KW fermions in this material. Our results suggest that a deeper theoretical and experimental investigation of helicity-dependent ARPES in the ordered phase could shed light on the exotic properties predicted for this Weyl-CDW compound. Our conclusions encourage the investigation of $(TaSe_4)_2I$ using spin-sensitive tools, such as spin-resolved ARPES and quantum interference, which can further confirm and provide insight into KW physics.

## Methods

### Sample preparation

Single crystals were prepared by adapting a chemical vapor transport technique reported by Maki et al.[29] Stoichiometric amounts of Ta wire (99.9%), Se powder (99.999%) and I shot (99.99%) were loaded into a fused silica tube, which was sealed under vacuum and heated with a source temperature of 600 °C and sink temperature of 500 °C for 10 days. XRD patterns were collected on a Bruker D8 ADVANCE diffractometer with Mo *Kα* radiation. Resistivity was measured in four-point geometry in a quantum design physical property measurement system.

### Density-functional theory

We perform fully relativistic, non-collinear first-principles DFT[62] simulations, including the spin-orbit interaction, using the Vienna Ab-Initio Simulation Package (VASP)[63–66]. We converted the atomic coordinates of the conventional unit cell of $(TaSe_4)_2I$ provided by Materials Project (mpID 30531)[67,68] to a primitive unit cell using AFLOW/ACONVASP[69]. The generalized-gradient approximation (GGA) as parameterized by Perdew, Burke, and Ernzerhof (PBE)[70] was used to describe exchange and correlation. Kohn-Sham states were expanded into a plane-wave basis with a kinetic-energy cutoff of 520 eV. A 10 × 10 × 10 Γ-centered Monkhorst-Pack grid[71] was used for BZ sampling, and the resulting Kohn-Sham Hamiltonian was diagonalized on finely sampled high-symmetry lines in reciprocal space

to obtain the electronic structure data in this work. In Fig. 3 in the main text, we visualized the electronic potential energy isosurface for several energies. For the plot, we compute the Kohn-Sham eigenvalues $\varepsilon_{n,k}$, where $n$ is the band index of the highest valence and the lowest conduction band, for the conventional unit cell. Further details are provided in the Supplementary Information[46].

### Single crystal X-ray scattering

Single crystal X-ray scattering measurements were carried out using the in-lab X-ray instrument equipped with a Xenocs GeniX3D Mo K$\alpha$ microspot X-ray source with multilayer focusing optics, providing $2.5 \times 10^7$ photons/sec in a beam spot of 130 μm at the sample position. The samples were cooled by a closed-cycle helium cryostat with a base temperature of 8 K mounted to a Huber four-circle diffractometer. The momentum resolution varied between $\Delta q = 0.01$ and 0.08 Å$^{-1}$ depending on the location in momentum space. Scattering signals were collected by a Mar345 image plate detector with 3450 × 3450 pixels. Three-dimensional surveys of momentum space were performed by taking images in 0.05° increments while sweeping samples through an angular range of 20° and mapping each pixel to the corresponding location in momentum space.

### Synchrotron ARPES

Measurements were performed using $p$-polarized 50 eV photons and a Scienta R4000 energy analyzer with a step size of 15 meV at Beamline 10.0.1.1, Advanced Light Source. The $(TaSe_4)_2I$ crystal was cleaved in-situ in an ultra high vacuum environment at room temperature. The analyzer slit was set parallel to the ΓZ direction.

### Laser ARPES

The light helicity-dependent ARPES measurements were performed using a hemispherical analyzer with electronic deflection (Scienta Omicron, DA30-L) to map both $k_x$ and $k_y$ without sample rotation. The photon energy was set to 6 eV (206 nm) using a custom-built setup that generated the 5th harmonic of a 1030 nm beam from a Yb-based laser source (Light Conversion PHAROS). The plane of incidence is set to the $k_n$-$k_\perp$ plane with a 45° incident angle (see Fig. S3 in ref. 46). The light helicity was adjusted with a quarter waveplate. The entrance slit of the hemispherical analyzer was parallel to the chain direction of the sample. This system has energy and momentum resolutions better than 10 meV and 0.002 Å$^{-1}$, respectively.

### Tight-binding modeling

The incoming wavefunction used in the theoretical modeling of the ARPES intensities was calculated using a tight-binding model with a large finite slab. Using $N$ to quantify the number of supercells, this model consists of an effective vacuum region of finite size $N$, followed by the interior of the slab of finite size $N$, followed by another effective vacuum region of finite size $N$. We chose $N = 30$ such that the initial state wavefunctions were sufficiently bulk-like, and so that the ARPES matrix element would approximate that of a semi-infinite slab. To emulate the rapid decay of the initial state wavefunction into the vacuum region, we set a large chemical potential of $\mu = 100$ eV in the vacuum zones and $\mu = 0$ in the interior zone. The final state was constructed as an approximate TR-LEED state.

## Data availability

All relevant data are available from the corresponding authors (bbradlyn@illinois.edu or fahad@illinois.edu) upon reasonable request.

## Code availability

The DFT simulation used the Vienna Ab-Initio Simulation Package (VASP) which is available at https://vasp.at. Codes used to analyze the ARPES data and implement the tight binding models are available from the corresponding authors (bbradlyn@illinois.edu or fahad@illinois.edu).

Received: 24 February 2025; Accepted: 12 September 2025;
Published online: 20 October 2025

## References

1. Fu, L., Kane, C. L. & Mele, E. J. Topological insulators in three dimensions. *Phys. Rev. Lett.* **98**, 106803 (2007).
2. Xia, Y. et al. Observation of a large-gap topological-insulator class with a single Dirac cone on the surface. *Nat. Phys.* **5**, 398 (2009).
3. Liu, Z. et al. Discovery of a three-dimensional topological Dirac semimetal, $Na_3Bi$. *Science* **343**, 864–867 (2014).
4. Liu, Z. et al. A stable three-dimensional topological Dirac semimetal $Cd_3As_2$. *Nat. Mater.* **13**, 677–681 (2014).
5. Lv, B. et al. Experimental discovery of Weyl semimetal TaAs. *Phys. Rev. X* **5**, 031013 (2015).
6. Lv, B. Q. et al. Observation of Weyl nodes in TaAs. *Nat. Phys.* **11**, 724–727 (2015).
7. Xu, S.-Y. et al. Discovery of a weyl fermion state with fermi arcs in niobium arsenide. *Nat. Phys.* **11**, 748–754 (2015).
8. Xu, S.-Y. et al. Discovery of a Weyl fermion semimetal and topological Fermi arcs. *Science* **349**, 613–617 (2015).
9. Bradlyn, B. et al. Beyond Dirac and Weyl fermions: unconventional quasiparticles in conventional crystals. *Science* **353**, aaf5037 (2016).
10. Chang, G. et al. Unconventional chiral fermions and large topological fermi arcs in RhSi. *Phys. Rev. Lett.* **119**, 206401 (2017).
11. Sanchez, D. S. et al. Topological chiral crystals with helicoid-arc quantum states. *Nature* **567**, 500–505 (2019).
12. Rao, Z. et al. Observation of unconventional chiral fermions with long Fermi arcs in CoSi. *Nature* **567**, 496–499 (2019).
13. Schröter, N. B. et al. Chiral topological semimetal with multifold band crossings and long Fermi arcs. *Nat. Phys.* **15**, 759–765 (2019).
14. Schröter, N. B. et al. Observation and control of maximal Chern numbers in a chiral topological semimetal. *Science* **369**, 179–183 (2020).
15. Vergniory, M., Elcoro, L., Felser, C., Bernevig, B. & Wang, Z. The (high quality) topological materials in the world. *Nature* **566**, 480–485 (2019).
16. Tang, F., Po, H. C., Vishwanath, A. & Wan, X. Efficient topological materials discovery using symmetry indicators. *Nat. Phys.* **15**, 470–476 (2019).
17. Zhang, T. et al. Catalogue of topological electronic materials. *Nature* **566**, 475–479 (2019).
18. Armitage, N. P., Mele, E. J. & Vishwanath, A. Weyl and Dirac semimetals in three-dimensional solids. *Rev. Mod. Phys.* **90**, 015001 (2018).
19. Wieder, B. J. et al. Topological materials discovery from crystal symmetry. *Nat. Rev. Mater.* **7**, 196–216 (2021).
20. Chang, G. et al. Topological quantum properties of chiral crystals. *Nat. Mater.* **17**, 978–985 (2018).
21. Flicker, F. et al. Chiral optical response of multifold fermions. *Phys. Rev. B* **98**, 155145 (2018).
22. Rees, D. et al. Helicity-dependent photocurrents in the chiral Weyl semimetal RhSi. *Sci. Adv.* **6**, eaba0509 (2020).
23. De Juan, F., Grushin, A. G., Morimoto, T. & Moore, J. E. Quantized circular photogalvanic effect in Weyl semimetals. *Nat. Comm.* **8**, 15995 (2017).
24. Ni, Z. et al. Linear and nonlinear optical responses in the chiral multifold semimetal RhSi. *npj Quantum Mater.* **5**, 96 (2020).
25. Zhang, C.-L. et al. Ultraquantum magnetoresistance in the Kramers-Weyl semimetal candidate $\beta$-$Ag_2Se$. *Phys. Rev. B* **96**, 165148 (2017).
26. Wan, B. et al. Theory for the negative longitudinal magnetoresistance in the quantum limit of Kramers Weyl semimetals. *J. Condens. Matter Phys.* **30**, 505501 (2018).
27. Ni, Z. et al. Giant topological longitudinal circular photo-galvanic effect in the chiral multifold semimetal CoSi. *Nat. Comm.* **12**, 154 (2021).
28. Wang, Z. Z. et al. Charge density wave transport in $(TaSe_4)_2I$. *Solid State Commun.* **46**, 325–328 (1983).

29. Maki, M., Kaiser, M., Zettl, A. & Grüner, G. Charge density wave transport in a novel inorganic chain compound $(TaSe_4)_2I$. *Solid State Commun.* **46**, 497–500 (1983).
30. Shi, W. et al. A charge-density-wave topological semimetal. *Nat. Phys.* **17**, 381–387 (2021).
31. Gooth, J. et al. Axionic charge-density wave in the Weyl semimetal $(TaSe_4)_2I$. *Nature* **575**, 315–319 (2019).
32. Wang, Z. & Zhang, S.-C. Chiral anomaly, charge density waves, and axion strings from Weyl semimetals. *Phys. Rev. B* **87**, 161107 (2013).
33. Sinchenko, A. A., Ballou, R., Lorenzo, J. E., Grenet, T. & Monceau, P. Does $(TaSe_4)_2I$ really harbor an axionic charge density wave? *Appl. Phys. Lett.* **120**, 063102 (2022).
34. Crepaldi, A. et al. Optically induced changes in the band structure of the weyl charge-density-wave compound $(TaSe_4)_2I$. *J. Phys. Mater.* **5**, 044006 (2022).
35. Nguyen, Q. L. et al. Ultrafast x-ray scattering reveals composite amplitude collective mode in the weyl charge density wave material $(TaSe_4)_2I$. *Phys. Rev. Lett.* **131**, 076901 (2023).
36. Kim, S. et al. Observation of a massive phason in a charge-density-wave insulator. *Nat. Mater.* **22**, 429–433 (2023).
37. Lin, M.-K. et al. Unconventional spectral gaps induced by charge density waves in the weyl semimetal $(TaSe_4)_2I$. *Nano Lett.* **24**, 8778 (2024).
38. Christensen, J. A. et al. Disorder and diffuse scattering in single-chirality $(TaSe_4)_2I$ crystals. *Phys. Rev. Mater.* **8**, 034202 (2024).
39. Yi, H. et al. Surface charge induced dirac band splitting in a charge density wave material $(TaSe_4)_2I$. *Phys. Rev. Res.* **3**, 013271 (2021).
40. Grüner, G. The dynamics of charge-density waves. *Rev. Mod. Phys.* **60**, 1129–1181 (1988).
41. Voit, J. Electronic structure of solids with competing periodic potentials. *Science* **290**, 501–503 (2000).
42. Tournier-Colletta, C. et al. Electronic instability in a zero-gap semiconductor: the charge-density wave in $(TaSe_4)_2I$. *Phys. Rev. Lett.* **110**, 236401 (2013).
43. van Smaalen, S., Lam, E. J. & Lüdecke, J. Structure of the charge-density wave in $(TaSe_4)_2I$. *J. Phys.:Condens. Matter* **13**, 9923 (2001).
44. Bradlyn, B. et al. Topological quantum chemistry. *Nature* **547**, 298–305 (2017).
45. Vergniory, M.G. et al. All topological bands of all nonmagnetic stoichiometric materials. *Science* **376**, 816 (2022).
46. See Supplementary Information.
47. Favre-Nicolin, V. et al. Structural evidence for ta-tetramerization displacements in the charge-density-wave compound $(TaSe_4)_2I$ from x-ray anomalous diffraction. *Phys. Rev. Lett.* **87**, 015502 (2001).
48. Fujishita, H., Shapiro, S. M., Sato, M. & Hoshino, S. A neutron scattering study of the quasi-one-dimensional conductor $(TaSe_4)_2I$. *J. Phys. C Solid State Phys.* **19**, 3049–3057 (1986).
49. Li, X.-P. et al. Type-III Weyl semimetals: $(TaSe_4)_2I$. *Phys. Rev. B* **103**, L081402 (2021).
50. Perfetti, L. et al. Spectroscopic indications of polaronic carriers in the quasi-one-dimensional conductor $(TaSe_4)_2I$. *Phys. Rev. Lett.* **87**, 216404 (2001).
51. Dardel, B. et al. Unusual photoemission spectral function of quasi-one-dimensional metals. *Phys. Rev. Lett.* **67**, 3144 (1991).
52. Gatti, G. et al. Radial spin texture of the Weyl fermions in chiral tellurium. *Phys. Rev. Lett.* **125**, 216402 (2020).
53. Sakano, M. et al. Radial spin texture in elemental tellurium with chiral crystal structure. *Phys. Rev. Lett.* **124**, 136404 (2020).
54. Wang, Y. H. et al. Observation of a warped helical spin texture in $Bi_2Se_3$ from circular dichroism angle-resolved photoemission spectroscopy. *Phys. Rev. Lett.* **107**, 207602 (2011).
55. Fu, L. Hexagonal warping effects in the surface states of the topological insulator $Bi_2Te_3$. *Phys. Rev. Lett.* **103**, 266801 (2009).
56. Jung, W. et al. Warping effects in the band and angular-momentum structures of the topological insulator $Bi_2Te_3$. *Phys. Rev. B* **84**, 245435 (2011).
57. Ryu, H. et al. Photon energy dependent circular dichroism in angle-resolved photoemission from Au(111) surface states. *Phys. Rev. B* **95**, 115144 (2017).
58. Crepaldi, A. et al. Momentum and photon energy dependence of the circular dichroic photoemission in the bulk rashba semiconductors BiTeX (X=I, Br, Cl). *Phys. Rev. B* **89**, 125408 (2014).
59. Liu, Y., Bian, G., Miller, T. & Chiang, T.-C. Visualizing electronic chirality and berry phases in graphene systems using photoemission with circularly polarized light. *Phys. Rev. Lett.* **107**, 166803 (2011).
60. Zhang, Y., Lin, L.-F., Moreo, A., Dong, S. & Dagotto, E. First-principles study of the low-temperature charge density wave phase in the quasi-one-dimensional Weyl chiral compound $(TaSe_4)_2I$. *Phys. Rev. B* **101**, 174106 (2020).
61. Lorenzo, J. E. et al. A neutron scattering study of the quasi-one-dimensional conductor $(TaSe_4)_2I$. *J. Phys. Condens. Matter* **10**, 5039 (1998).
62. Hohenberg, P. & Kohn, W. Inhomogeneous electron gas. *Phys. Rev.* **136**, B864 (1964).
63. Kresse, G. & Furthmüller, J. Efficient iterative schemes for ab initio total-energy calculations using a plane-wave basis set. *Phys. Rev. B* **54**, 11169 (1996).
64. Kresse, G. & Joubert, D. From ultrasoft pseudopotentials to the projector augmented-wave method. *Phys. Rev. B* **59**, 1758–1775 (1999).
65. Gajdoš, M., Hummer, K., Kresse, G., Furthmüller, J. & Bechstedt, F. Linear optical properties in the projector-augmented wave methodology. *Phys. Rev. B* **73**, 045112 (2006).
66. Steiner, S., Khmelevskyi, S., Marsmann, M. & Kresse, G. Calculation of the magnetic anisotropy with projected-augmented-wave methodology and the case study of disordered $Fe_{1-x}Co_x$ alloys. *Phys. Rev. B* **93**, 224425 (2016).
67. Jain, A. et al. The materials project: a materials genome approach to accelerating materials innovation. *APL Mater.* **1**, 011002 (2013).
68. Ong, S. P. et al. Python Materials Genomics (pymatgen): a robust, open-source python library for materials analysis. *Comput. Mater. Sci.* **68**, 314–319 (2013).
69. Setyawan, W. & Curtarolo, S. High-throughput electronic band structure calculations: challenges and tools. *Comput. Mater. Sci.* **49**, 299–312 (2010).
70. Perdew, J. P., Burke, K. & Ernzerhof, M. Generalized gradient approximation made simple. *Phys. Rev. Lett.* **77**, 3865 (1996).
71. Monkhorst, H. J. & Pack, J. D. Special points for brillouin-zone integrations. *Phys. Rev. B* **13**, 5188 (1976).
72. Momma, K. & Izumi, F. VESTA3 for three-dimensional visualization of crystal, volumetric and morphology data. *J. Appl. Crystallogr.* **44**, 1272–1276 (2011).


## Acknowledgements

We thank Benjamin Wieder for fruitful discussions. This study was supported by the Center for Quantum Sensing and Quantum Materials, an Energy Frontier Research Center funded by the U.S. Department of Energy, Office of Science, Basic Energy Sciences under Award DE-SC0021238. This research used resources of the Advanced Light Source (ALS), which is a DOE Office of Science User Facility under Contract No. DE AC02 05CH11231. F.M. acknowledges support from the EPiQS program of the Gordon and Betty Moore Foundation, Grant GBMF11069. NB and AS acknowledge support from the Illinois Materials Research Science and Engineering Center, supported by the National Science Foundation MRSEC program under NSF Award No. DMR-1720633. S.K. was supported by the DGIST Start-up Fund (No. 2025010016) and R&D Program (No. 2025060028) of the Ministry of Science and ICT. This work made use of the Illinois Campus Cluster, a computing resource that is operated by the Illinois Campus Cluster Program (ICCP) in conjunction with the National Center for Supercomputing Applications (NCSA) and which is supported by funds from the University of Illinois at Urbana-Champaign. The crystal structure plotted in Fig. 1a was generated with the VESTA software[72].

## Author contributions

S.K., N.B. and F.M. performed the laser-ARPES experiments and the corresponding data analysis. R.C.M and B.B. developed the theoretical methods, the tight-binding model and the theoretical analysis. J.P. and A.S. developed and carried out the DFT simulations. C.Z. and D.P.S synthesized the samples and performed the four terminal resistivity measurements. M-K.L., J.A.H., S-K.M. and T.-C.C. performed the synchrotron ARPES experiments. X.G. and P.A. carried out the XRD measurements. S.K., R.C.M, B.B. and F.M. wrote the manuscript with input from all the authors. This project was supervised and directed by B.B. and F.M.

## Competing interests

The authors declare no competing interests.

## Additional information

**Supplementary information** The online version contains supplementary material available at https://doi.org/10.1038/s43246-025-00952-7.

**Correspondence** and requests for materials should be addressed to Barry Bradlyn or Fahad Mahmood.

**Peer review information** *Communications Materials* thanks the anonymous reviewers for their contribution to the peer review of this work. Primary Handling Editors: [EBM name(s)] and [Internal Editor name(s)] [A peer review file is available].